Dalton Transactions

ROYAL SOCIETY OF CHEMISTRY

PAPER

View Article Online
View Journal | View Issue

Cite this: *Dalton Trans.*, 2025, **54**, 9517

The role of an LMCT state on luminescence quenching in dimeric lanthanide dipivaloylmethanate compounds†

Paulo R. S. Santos,[a] Ashely A. S. S. Jesus,[a] William B. Lima,[a] Iran F. Silva,[a] Joaldo G. Arruda,[a] Wagner M. Faustino,[a] Maria Claudia F. C. Felinto,[b] Hermi F. Brito,[c] Israel F. Costa,[c] Renata Diniz[d] and Ercules E. S. Teotonio *[a]

A series of four dimeric lanthanide dipivaloylmethanate (dpm) compounds with bis(diphenylphosphine) ethane oxide ($dppeO_2$) as an ancillary ligand having the formula $[Ln_2(dpm)_6(dppeO_2)]$ (Ln^{3+}: Sm^{3+}, Eu^{3+}, Gd^{3+}, and Tb^{3+}) have successfully been synthesized. Single-crystal X-ray diffraction analysis shows that dimeric compounds crystallize in the $P\bar{1}$ space group. Furthermore, the first coordination sphere $\{LnO_7\}$ of each Ln^{3+} ion can be described as a capped octahedron with a distorted C_{3v} symmetry site. Photoluminescence data show that the Tb^{3+} compound exhibits high emission intensity consistent with an efficient intramolecular energy transfer from the dpm organic ligand to the metal ion. However, the analogous Eu^{3+} and Sm^{3+} compounds display only weak emission intensities under excitation upon the ligand $S_0 \rightarrow S_1$ transition, reflecting efficient luminescence quenching *via* a low-energy ligand-to-metal charge transfer (LMCT) state and metal-to-ligand energy back transfer, respectively. For the $[Eu_2(dpm)_6(dppeO_2)]$ compound, the photophysical properties based on the radiative rate (A_{rad}), the non-radiative rate (A_{nrad}), and the Judd–Ofelt intensity parameters ($\Omega_{2,4}$) were also investigated. Besides, theoretical studies were performed in the DFT and TD-DFT levels in conjunction with the JoySpectra platform, yielding a deeper understanding of the intramolecular energy transfer processes. The highest value of the energy transfer rate (W) assigned to the $S_1 \rightarrow$ LMCT deactivation pathway compared to the rate values from the $^5D_0$ or $^5D_1 \rightarrow$ LMCT channels agrees well with the experimental values of the intrinsic (Q^{Eu}_{Eu}) and extrinsic (Q^{L}_{Eu}) quantum yields. These optical results indicated that the LMCT state plays the most critical role in Eu–dpm luminescence quenching by depopulating the excited S_1 ligand state.

Received 25th January 2025,
Accepted 10th May 2025

DOI: 10.1039/d5dt00203f

rsc.li/dalton

1 Introduction

Luminescent coordination compounds containing lanthanide ions are among the materials of most significant interest for applications in technological devices such as optical fibers, LEDs, and luminescent thermometer device displays due to their exceptional spectroscopic properties.[1–3] In particular, their photophysical features depend on the electronic energy structures of Ln^{3+} ions. Intraconfigurational-4f transitions prohibited by Laporte's selection rule present very low values of oscillator strength ($P \sim 10^{-6}$). In this case, the luminescence sensitization process of the Ln^{3+} ion *via* organic ligands is one of the key factors driving intensive theoretical and experimental investigations on these materials. As is well known, this is one of the strategies to overcome the very low absorption and emission intensities when the lanthanide is directly excited.[4]

β-Diketone ligands may act as efficient photon absorbers among organic molecule classes due to their high molar coefficient absorptivities. Furthermore, these ligands may contribute to a very efficient intramolecular energy transfer process, which depends on the energy positions of the lower energy singlet (S_1) and triplet (T_1) excited states belonging to the ligand relative to the excited energy levels ($^{2S+1}L_J$) of the Ln^{3+} ion. By taking this into account, several luminescence sensitization mechanisms have been proposed in the literature,[5] highlighting the nonradiative energy transfer processes among these excited ligand states. However, intensive theoretical studies have shown that the pathway involving the low-lying T_1

[a]Department of Chemistry - University Federal of Paraíba, 58051-970 João Pessoa, PB, Brazil. E-mail: teotonioees@quimica.ufpb.br
[b]Nuclear and Energy Research Institute–IPEN/CNEN, 05508-900 São Paulo, SP, Brazil
[c]Department of Fundamental Chemistry - Institute of Chemistry of the University of São Paulo, 05508-900 São Paulo, SP, Brazil
[d]Department of Chemistry, ICEx, University of Minas Gerais, Belo Horizonte, MG, 31270-901, Brazil

†Electronic supplementary information (ESI) available. CCDC 2362689–2362691. For ESI and crystallographic data in CIF or other electronic format see DOI: https://doi.org/10.1039/d5dt00203f

state of the β-diketone ligand is paramount for understanding the luminescence properties of Ln^{3+} compounds with higher emission quantum yields.[6,7]

Although the electronic states of the organic ligands and the Ln^{3+} ion may meet the requirements for a very efficient luminescence sensitization process, luminescence quenching processes assigned to the multiphonon non-radiative relaxations, mainly those owing to high-energy X–H (X: C, N and O) vibrational modes, may significantly decrease the intrinsic quantum yield in the Ln^{3+} compounds.[8–11] Another significant quencher channel is through the ligand-to-metal charge transfer (LMCT) states of low energies. In particular, Eu^{3+} complexes have gained much attention because they exhibit well-defined emission bands in the visible spectral region, which are assigned to the 4f–4f transitions from the non-degenerate $^5D_0$ emitting level. However, these systems may have their luminescence intensities dependent on the position of the LMCT state.

In a systematic theoretical study, Faustino *et al.*[12] demonstrated that the luminescence quenching processes are more efficient in Eu^{3+} coordination compounds presenting LMCT excited states almost resonant with the low-lying excited T_1 state of the ligand or the excited $^5D_0$ and $^5D_1$ levels of the lanthanide ion. Moreover, for example, the temperature dependence on the relaxation rate of the $^5D_0$ level is observed in $Eu^{3+}(dpm)_3$ complexes.[13]

The strong luminescence quenching is associated with the energy transfer process between the emitting $^5D_0$ level and the LMCT state.[14] These results are supported by the photoluminescence investigation and positron annihilation spectroscopy of $Ln(dpm)_3(2\text{-pyr})$ complexes (Ln: Eu^{3+} and Tb^{3+} and 2-pyr: 2-pyrrodilidone).[15] Miranda *et al.*[16] reported the synthesis of a new compound $[Eu(dpm)_2(NO_3)(tppo)_2]$ and compared its photophysical properties with those of the dimeric homoleptical $[Eu_2(dpm)_6]$ compound. The luminescence properties of these Ln^{3+} complexes are determined by the positions of the LMCT state, which has the lowest energy in the dimeric compound and the highest energy in the monomeric compound.

Although LMCT states play an important role in luminescence quenching, the factors contributing to the presence of these states in the low-energy regions of lanthanide ion compounds are not yet fully understood. Recently, several studies have used TD-DFT theoretical calculations to investigate the electronic structure of these materials in order to provide insights into the experimental findings.

In the last decade, many works have been focused on the synthesis and photoluminescence study of Ln^{3+} $(\beta\text{-diketonato})_3$ compounds containing phosphine oxide bidentate ligands. Hasegawa *et al.* reported the temperature dependence on the luminescence properties of mixed Eu^{3+}/Tb^{3+} compounds with bidentate phosphine oxide ligands, and the variation of emission color of the complex with temperature was associated with the presence of a low energy LMCT state.[15] These systems open up several possibilities for new luminescent compounds in which phosphine oxide can act as a bridging or chelating ligand, leading to polymeric or dimeric forms.[17–21]

In this study, we focus on the synthesis and spectroscopic investigation of $[Ln_2(dpm)_6(dppeO_2)]$ complexes {Ln: Sm^{3+}, Eu^{3+}, Tb^{3+}, and Gd^{3+}; where $dppeO_2$: bis(diphenylphosphine) ethane}. The structural properties of these compounds were analyzed using the single-crystal X-ray diffraction technique. In particular, the low Eu(III)/Eu(II) reduction potential ($E^\circ = -0.34$ V) associated with the high charge-donating capacity of the dpm ligand makes the $[Eu_2(dpm)_6(dppeO_2)]$ complex an excellent platform for investigating molecular systems with LMCT states of low energies. The photophysical behavior, taking into account the critical role of the ligand–metal charge transfer (LMCT) state in the ligand-to-metal intramolecular energy transfer process of Ln^{3+} coordination compounds, has also been investigated.

2 Experimental

All experimental procedures were performed using analytical grade reagents. The chemicals used were as follows: ethanol (C_2H_6O, Tedia, 99.3%), methanol (CH_4O, Tedia, 99.8%), chloride acid (HCl, Alfa Aesar, 28%), 1,2-bis(diphenylphosphino) ethane ($C_{26}H_{28}P_2$, Sigma-Aldrich, 99%), hydrogen peroxide solution (H_2O_2, VETEC, 30%), 2,2,6,6-tetramethyl-3,5-heptanedionate ($C_{11}H_{20}O_2$, Sigma-Aldrich, 98%), ethylenediaminetetraacetic acid (EDTA, Sigma-Aldrich, 99.5%), europium oxide (Eu_2O_3, Sigma-Aldrich, 99.999%), gadolinium oxide (Gd_2O_3, Alfa Aesar, 99.999%), terbium oxide (Tb_2O_3, Sigma-Aldrich, 99.999%) and samarium oxide (Sm_2O_3 Aldrich, 99.999%).

Unlike the traditional method used in the preparation of lanthanide dimeric compounds that employs aqua-complexes as precursors,[22] the compounds were obtained by the direct reaction between the organic ligands (dpm and $dppeO_2$) and the salts of Ln^{3+} ions. To an ethanol solution containing 0.150 g (0.814 mmol) of dipivaloylmethanate and 0.116 g (0.271 mmol) of 1,2-bis(diphenylphosphine)ethane oxide ($dppeO_2$), NH_4OH (0.1 mol L^{-1}) was added dropwise until the pH ~ 7.0 under stirring. Subsequently, the resulting solution was added dropwise to an ethanol solution containing 0.110 g (0.271 mmol) of $LnCl_3{\cdot}6H_2O$. After that, the pH of the homogeneous solution was adjusted again to ~7.0 (Scheme 1). Therefore, the reaction system was allowed to stand for 2 days at room temperature, yielding colorless single crystals. Finally, these crystals were washed with cold ethanol and dried under environmental conditions.

The characterization data for the $[Ln_2(dpm)_6(dppeO_2)]$ compounds (Ln = Sm^{3+}, Eu^{3+}, Gd^{3+}, and Tb^{3+}) obtained from elemental analysis and infrared spectroscopy are presented below:

$[Sm_2(dpm)_6(dppeO_2)]$ – Yield: 130.70 mg (65%). FT-IR (in KBr/cm^{-1}): 3052 (w), 2958 (w), 2904 (w), 2866 (w), 1573 (s), 1539 (s), 1504 (s), 1404 (s), 1357(s), 1222(s), 1176 (s), 1138 (m) 867 (m), 729 (m), 694 (m); 601 (m), 532 (w) 509 (w), 474 (w). calcd: C, 60.36; H, 7.60; Sm, 16.43%, found: C, 60.78; H, 7.65; Sm, 16.23%.

$[Eu_2(dpm)_6(dppeO_2)]$ – Yield: 145.10 mg (71%). FT-IR (in KBr/cm^{-1}): 3062 (w), 2958 (w), 2866 (w), 1573 (s), 1539 (s), 1504

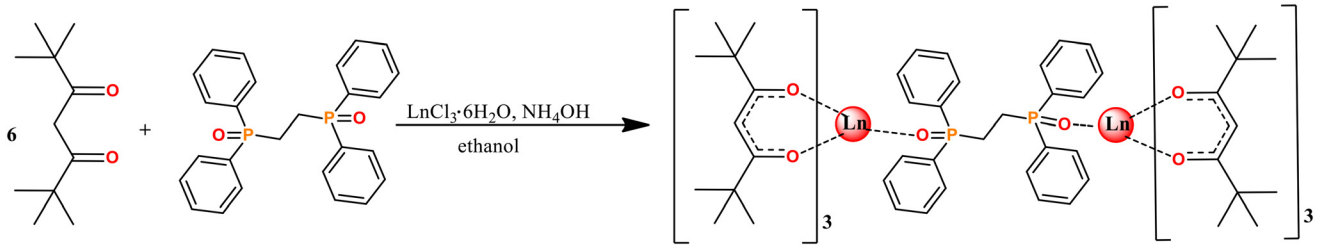

Scheme 1 Synthesis of $[Ln_2(dpm)_6(dppeO_2)]$ compounds **1–4** using Sm^{3+}, Eu^{3+}, Gd^{3+} and Tb^{3+} ions, respectively.

(s), 1400 (s), 1357(s), 1226(m), 1195 (m), 1180 (m), 1138 (m) 933 (m), 729 (m), 694 (m); 601 (m), 532 (w) 509 (w), 474 (w). calcd: C, 60.25; H, 7.58; Eu, 16.57%, found: C, 60.81; H, 7.65; Eu, 16.56%.

$[Gd_2(dpm)_6(dppeO_2)]$ – Yield: 155.46 mg (69%). FT-IR (in KBr/cm^{-1}): 3052 (w), 2958 (w), 2904 (w), 2866 (w), 1573 (s), 1539 (s), 1504 (s), 1404 (s), 1357(s), 1222(s), 1176 (s), 1138 (m) 867 (m), 729 (m), 694 (m); 601 (m), 532 (w) 509 (w), 474 (w). calcd: C, 59.91; H, 7.54; Gd, 17.05%, found: C, 58.90; H, 7.40; Gd, 17.28%.

$[Tb_2(dpm)_6(dppeO_2)]$ – Yield: 150.70 mg (77%). FT-IR (in KBr/cm^{-1}): 3058 (w), 2958 (w), 2866 (w), 1573 (s), 1539 (s), 1504 (s), 1411 (s), 1357(s), 1226(m), 1199 (m), 1180 (m), 1138 (m) 867 (m), 790 (m), 729 (m); 694 (m), 601 (w) 532 (w), 509 (w), 474 (w). calcd: C, 59.80; H, 7.53; Tb, 17.20%, found: C, 58.93; H, 7.32; Tb, 17.67%.

The formulas of the compounds were estimated from the percentage data of Ln^{3+} ions obtained by complexometric titrations with a standardized EDTA solution and using xylenol orange as an indicator and from the percentages of C, H and N determined using a Perkin Elmer 2400 series II analyzer. The coordination modes of the ligands in the compound were investigated by Fourier transform infrared (FTIR) spectra, in the range of 4000–400 cm^{-1}, using a Shimadzu spectrophotometer, model IRPrestige-21. In this case, approximately 0.100 g of the sample was dispersed in a KBr pellet and the absorption spectra were recorded with an average of 45 accumulations and 4 cm^{-1} spectral resolution. Thermogravimetric analyses were performed in the 25–900 °C temperature range employing a Shimadzu DTG-60 instrument under a dynamic nitrogen atmosphere at heating rates of 50 mL min^{-1} and 10 °C min^{-1}. Diffuse reflectance spectra (DRS) of the complexes diluted with $BaSO_4$ were recorded between 190 and 600 nm with a Shimadzu UV2600i UV-VIS spectrophotometer using an integrating sphere coated with the $BaSO_4$ compound. The steady-state excitation and emission spectra were recorded at room temperature. Appropriate single crystals of the $[Ln_2(dpm)_6(dppeO_2)]$ compounds (Ln: Eu^{3+}, Gd^{3+}, and Tb^{3+}) for collecting X-ray diffraction data were mounted on a SuperNova Rigaku diffractometer operating with a Mo-Kα (λ = 0.71073 Å) radiation source at 293 K. X-ray diffraction data, cell refinements, and corrections for intensity and polarization effects were performed using CrysAlisPro software.[23] All structures were solved and refined with the OLEX2[24] suite using SHELX programs.[25] The figures were generated using ORTEP3 for Windows,[25] POV-RAY[26] and VESTA.[27]

The experimental luminescence data, including steady-state excitation and emission spectra, were collected with samples in a quartz tube using a HORIBA Fluorolog-3 (FL22) spectrofluorometer, in which a 450 W Xenon lamp and a R928P PMT photomultiplier were used as the excitation source and detector, respectively. The luminescence decay curves were recorded using the same equipment, but a pulsed lamp was used as the excitation source. The extrinsic quantum yields of the complexes in the solid state were determined using a QuantaPhi-2 integrating sphere coupled to a HORIBA Fluorolog-QM™ spectrofluorimeter.

3 Results and discussion

3.1 Characterization of the Ln^{3+} complexes

Structural investigation of the Ln^{3+} compounds. The structures of the $[Ln_2(dpm)_6(dppeO_2)]$ compounds, Ln: Eu^{3+}, Gd^{3+} and Tb^{3+}, were elucidated by the X-ray diffraction single crystal method. The crystal collection parameters and refinement data for the compound (Table 1) suggest that all investigated compounds are isomorphous and crystallize in the triclinic space group $P\bar{1}$ with a value of Z = 2. This similar structural finding is probably due to lanthanide ions presenting the same oxidation states (+3) and similar ionic radii. Furthermore, all coordination compounds present two symmetrical $Ln(dpm)_3$ units connected by a bridging $dppeO_2$ ligand, as illustrated in Fig. 1. These structural results are in agreement with those reported by Yan and co-workers[28] for the analog Dy^{3+} complex. The chemical environment of each Ln^{3+} ion in the first heptacoordinated sphere $\{LnO_7\}$ presents 6 oxygen atoms from three bidentate chelating dpm ligands (O1–O6) and an oxygen atom (O7) from the $dppeO_2$ ligand. Notably, dpm ligands in these compounds are not symmetrically coordinated with the Ln^{3+} ions, for example, the Eu–O1 and Eu–O2 bond lengths are equal to 2.404(2) and 2.337(2) Å, respectively. A comparison among the structural data for different compounds reveals a decrease in the Ln^{3+}–O=P bond distances in the following trend for the different Ln^{3+} ions: Eu^{3+} 2.351(2) Å > Gd^{3+} 2.311(2) Å > Tb^{3+} 2.298(2) Å. This behavior also reflects the decrease in the ionic radii of the Ln^{3+} ion.[29] The bond angles (O–Ln–O) and bond distances (Ln–O)

Table 1 Structural data of the $[Ln_2(dpm)_6(dppeO_2)]$ compounds (Ln: Eu^{3+}, Gd^{3+}, and Tb^{3+}) elucidated by the X-ray diffraction single-crystal method

Parameters	$[Eu_2(dpm)_6(dppeO_2)]$	$[Gd_2(dpm)_6(dppeO_2)]$	$[Tb_2(dpm)_6(dppeO_2)]$
Crystal formula	$C_{46}H_{69}O_7PEu$	$C_{46}H_{69}O_7PGd$ (**3**)	$C_{46}H_{69}O_7PTb$ (**4**)
MM (g mol^{-1})	916.94	922.23	923.90
Crystalline system	Triclinic	Triclinic	Triclinic
Space group	$P\bar{1}$	$P\bar{1}$	$P\bar{1}$
a (Å)	10.4877(2)	13.2868(1)	13.2634(1)
b (Å)	13.5301(2)	14.0175(1)	13.9923(1)
c (Å)	19.12302(3)	15.1758(2)	15.1852(1)
α (°)	77.794(1)	84.7110(10)	84.9401(7)
β (°)	76.760(1)	86.0780(10)	86.2469(8)
γ (°)	71.063(1)	62.2230(10)	62.2765(10)
V (Å^3)	2471.52(6)	2489.07(5)	2483.96(4)
Temperature (K)	293(2)	293(2)	293(2)
Z	2	2	2
$D_{calc.}$ (g cm^{-3})	1.232	1.230	1.235
Crystal size	0.15 × 0.39 × 0.50	0.10 × 0.34 × 0.47	0.11 × 0.36 × 0.48
μ(Mo Kα) (cm^{-1})	1.350	9.270	7.6600
Measured/unique reflections	69 163/13 336	52 100/10 603	52 396/10 594
R_{int}	0.0441	0.0643	0.0504
Observed reflections $[F_o^2 > 2\sigma(F_o^2)]$	11 407	9812	9843
Refined parameters	515	520	520
$R_{obs}[F_o > 2\sigma(F_o)]$	0.0345	0.0425	0.0348
R_{all}	0.0444	0.0452	0.0373
wR_{obs} $[F_o^2 > 2\sigma(F_o)^2]$	0.0859	0.1050	0.0913
wR_{all}	0.0904	0.1069	0.0930
S	1.037	1.025	1.033

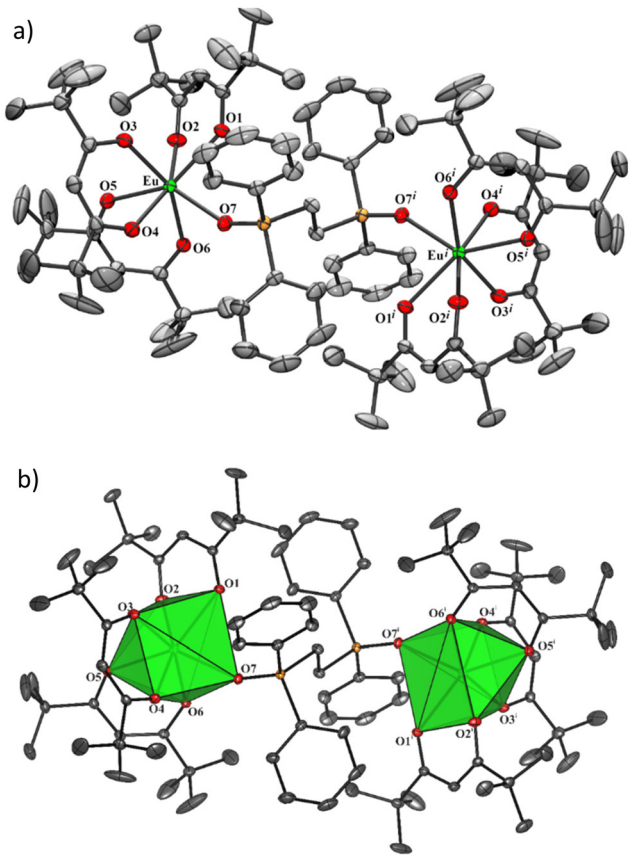

Fig. 1 (a) ORTEP representation of the structural data for the $[Eu_2(dpm)_6(dppeO_2)]$ compound and (b) the coordination polyhedron with the symmetry code (i: 1 − *x*, 1 − *y*, and 1 − *z*).

are shown in more detail in Table S1†. It is also observed that the highest (9.165 Å) and the smallest (8.952 Å) Ln–Ln distances are found for the complexes containing the Eu^{3+} and Tb^{3+} ions, respectively.

The SHAPE program was used to estimate the coordination geometry of the Ln^{3+} compounds and quantify the distortion of the coordination spheres of the complexes.[30] The coordination polyhedron of the Eu^{3+} compound is a capped trigonal prism geometry (CTPR-7, C_{2v} symmetry group) with a deviation value of CShM = 0.724 (Table S2†). In the case of the dimeric compounds containing the Gd^{3+} and Tb^{3+} ions, the coordination polyhedral is defined as a capped octahedron geometry (COC-7, C_{3v}) with deviation values 0.537 and 0.499, respectively. It is worth mentioning that Dy^{3+}–dpm presents the lowest S = 0.467 value reported in ref. 28. This structural behavior suggests a tendency towards an increase in the symmetry of the chemical environment around the lanthanide ions from the C_{2v} to C_{3v} sites as the metal ion radius decreases. The lanthanide contraction effect is expected to lead to an excellent approximation between the organic ligands, increasing the steric hindrance among them and, in turn, promoting a more significant structural distortion of the chemical environment.[30] Most of the methyl groups of the dpm ligand are disordered in the structures. The better disorder model was the treatment in the group. The final major occupancy factors were 0.72, 0.63 and 0.65, respectively, for the $[Eu_2(dpm)_6(dppeO_2)]$, $[Gd_2(dpm)_6(dppeO_2)]$ and $[Tb_2(dpm)_6(dppeO_2)]$ compounds.

It is noteworthy that the crystallographic information files (CIFs) containing complete data on the structural studies have been deposited at the Cambridge Crystallographic Data Center

(CCDC) under numbers 2362689, 2362690, and 2362691† for Eu^{3+}, Gd^{3+}, and Tb^{3+}, respectively.

Thermogravimetric analysis. The thermogravimetric (TG) and differential thermal analysis (DTA) data of the dimeric coordination compounds $[Ln_2(dpm)_6(dppeO_2)]$ (Ln: Sm^{3+}, Eu^{3+}, $Gd^{3+}$and Tb^{3+}) (Fig. S1†) indicate similar thermal decomposition, stoichiometric and structural behaviors. Furthermore, Fig. S1† displays no thermal decomposition event before 200 °C, suggesting that the anhydrous dimeric compounds have high thermal stability. The first thermal event shown in the DTA curves is an endothermic peak at around 235 °C due to the melting processes (Table S3†). Above this temperature, TG curves exhibit the most pronounced mass loss event in the 240–380 °C temperature range, with a mass loss of ~79.2% of the initial mass. Interestingly, a stable intermediate product can be found in the range from 400 to 490 °C. After this interval, a second decomposition event occurs at 500–600 °C, corresponding to a total mass loss of around 13, 5, and 3% for the Eu^{3+}, Gd^{3+}, and Tb^{3+} compounds, respectively, indicating that the final residues correspond to the lanthanide oxides (Ln_2O_3). In particular, the final residue of thermal decomposition for the Sm^{3+} compound corresponds to 31.8%, which is consistent with the calculated value of 29.8% and in agreement with the formation of the samarium phosphate ($SmPO_4$). The FTIR spectral data of the residual material from the thermal decomposition of the $[Sm_2(dpm)_6(dppeO_2)]$ compound (Fig. S2†) agree with the proposal to form samarium phosphate.[31]

This result suggests that the first mass loss event (240–380 °C) may be assigned to the decomposition of the dimeric compound moiety by the evaporation of the $Ln(dpm)_3$ complex. Many lanthanide tris(dipivaloylmethanate) complexes of different stoichiometries reported in the literature have shown similar thermal behaviors.[15] In this case, the main remaining product from the first thermal decomposition step can be assigned to a lanthanide complex with the $dppeO_2$ ancillary ligand. Notably, even considering that the compounds have the exact stoichiometry, the final residue values decrease by 13.5 and 3% due to the decrease in the ionic radii of the Eu^{3+}, Gd^{3+}, and Tb^{3+} oxides.

Infrared absorption spectroscopy. The FTIR absorption spectra of the $[Ln_2(dpm)_6(dppeO_2)]$ compounds (Ln: Sm^{3+}, Eu^{3+}, Gd^{3+} and Tb^{3+}) recorded in the range of 4000–400 cm^{-1} (Fig. S3†) show characteristic absorption bands at approximately 2959 and 1574 cm^{-1}, which may be attributed to the δ(C–H) axial and ν(C═O and C═C) stretching modes of the dpm ligand, respectively. As compared with the spectra of the uncoordinated dpm ligand, these absorption bands are shifted to lower wavenumbers, indicating that the dpm ligand coordinates with the Ln^{3+} ion in chelating mode. The absorption peak observed at 3063 cm^{-1} corresponds to the ν(C–H) stretching mode of the $dppeO_2$ ancillary ligand. Furthermore, the absorption bands centered at 1175 and 1440 cm^{-1} may be assigned to the ν(P═O) and ν(P–C) stretching modes.[31]

3.2 Diffuse reflectance spectra of the Ln^{3+} complexes

Fig. 2 shows the diffuse reflectance spectra of the solid-state $[Ln_2(dpm)_6(dppeO_2)]$ compounds (Ln: Sm^{3+}, Eu^{3+}, Tb^{3+}, and Gd^{3+}) recorded in the spectral range from 200 to 600 nm. In general, these spectra are characterized by broad bands in the spectral range of 250–450 nm, which can be attributed to the $S_0 \rightarrow S_2$ and $S_0 \rightarrow S_1$ transitions that exhibit a strong $\pi \rightarrow \pi^*$ character centered on the dpm ligand. Besides these bands, the absorption spectra of the Sm^{3+} and Tb^{3+} compounds (Fig. S4†) also exhibit narrow bands assigned to the intraconfigurational $4f^5$ transitions of the Sm^{3+} ion from the ground $^6H_{5/2}$ level to the excited $^4F_{9/2}$ (363 nm), $^4L_{17/2}$ (375 nm), $^4F_{11/2}$ (390 nm) and $^4F_{7/2}$ (403 nm) levels. On the other hand, in the reflectance spectra of the Eu^{3+}, Tb^{3+}, and Gd^{3+} compounds, no narrowband related to the intraconfigurational transitions of the Ln^{3+} ions has been observed due to the high relative intensities of ligand absorption bands.

Due to the similarity between the reflectance spectra of the Eu^{3+} and Gd^{3+} compounds, a shoulder may be observed in the spectrum of the $[Eu_2(dpm)_6(dppeO_2)]$ compound in the longer wavelength region (Fig. 2). This additional band can be attributed to an electronic transition from the singlet ground state to the ligand–metal charge transfer (LMCT) state ($S_0 \rightarrow$ LMCT). As previously reported by Faustino *et al.*,[13] the LMCT state with energy in the range of 500–25 000 cm^{-1} can play a key role in quenching the Eu^{3+} luminescence by reducing the population of the emitting state of the metallic center. Our research group has intensively studied the effects of the LMCT state on the luminescence properties of β-detonate complexes.[15,32]

Although the characterization of LMCT states in lanthanide complexes is difficult due to their overlap with ligand absorption bands, the large band shift allowed a quantitative analysis to be carried out. In this case, the energy position of the low-

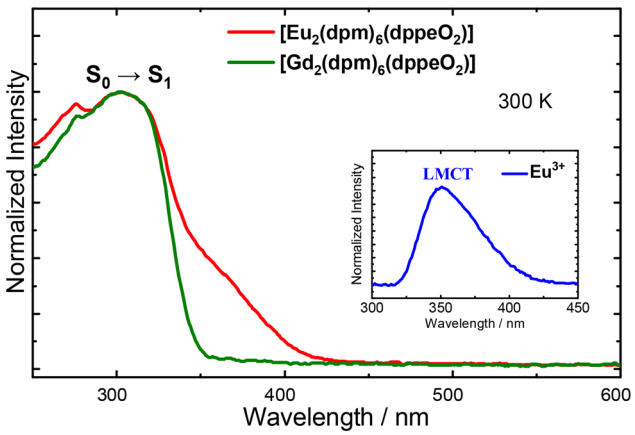

Fig. 2 Diffuse reflectance spectra of the $[Ln_2(dpm)_6(dppeO_2)]$ compounds (Ln: Eu^{3+} (red line) and Gd^{3+} (green line)). The experimental spectrum is shown in solid black lines. The inset figure shows the LMCT band (blue line) obtained by subtraction between the spectra from the Eu^{3+} and Gd^{3+} complexes. The insert photographs correspond to the Eu^{3+} (yellowish crystal) and Gd^{3+} (colorless crystal) complexes under ambient light.

lying LMCT state for the Eu^{3+} compound was determined from the deconvolution performed in the reflectance spectrum (Fig. 2) of the Eu compound, and the LMCT energy was determined using the Jacobian transform and the energy obtained from these data is equal to 29 154 cm^{-1} (Fig. S5†). In addition, the LMCT state can affect the antenna effect by overriding the low-level singlet or triplet excited states.

3.3 Photoluminescence properties

The energy position of the low-lying excited T_1 state of the dpm ligand in the $[Ln_2(dpm)_6(dppeO_2)]$ compounds was obtained from the time-resolved phosphorescence spectrum of the Gd^{3+} compound recorded at liquid nitrogen temperature (77 K) in the spectral range from 430 to 700 nm under excitation at 370 nm (Fig. S6†). In this case, a delay time of 1 ms was used to exclude contributions from the fluorescence band due to the $S_1 \rightarrow S_0$ transition. Similarly to the reflectance analysis, the phosphorescence spectrum was previously treated with the Jacobian transform to convert the data to a more appropriate scale. Thus, the barycenter of the $T_1 \rightarrow S_0$ transition equal to 20 089 cm^{-1} was determined using the Python code reported in ref. 9.

The excitation spectra of the $[Sm_2(dpm)_6(dppeO_2)]$ compound recorded at 298 and 77 K in the spectral range of 250–590 nm by monitoring the emission intensity of the $^4G_{5/2} \rightarrow {}^6H_{13/2}$ transition at 646 nm (Fig. 3a) show similar profiles, presenting broad excitation bands in the higher energy region assigned to the $S_0 \rightarrow S_n$ transition. Additionally, narrow excitation peaks observed from the characteristic Sm^{3+} transitions are as follows: $^6H_{5/2} \rightarrow {}^4H_{9/2}$ (345 nm), $^4F_{9/2}$ (363 nm), $^4L_{17/2}$ (375 nm), $^4F_{11/2}$ (390 nm), $^4F_{7/2}$ (403 nm), $^4M_{19/2}$ (417 nm), $^4I_{15/2}$ (442 nm), $^4F_{3/2}$ (452 nm), $^4I_{13/2}$ (463 nm), $^4I_{11/2}$ (478 nm), $^4G_{7/2}$ (499 nm), $^4F_{3/2}(2)$ (530 nm) and $^4G_{5/2}$ (560 nm). As noted, some narrow bands due to these intraconfigurational $4f^5$ transitions have higher relative intensity compared to the broadband of the $S_0 \rightarrow S_1$ ligand transition in both excitation spectra recorded at room temperature and low temperatures. These optical results suggest the low-efficiency intramolecular energy transfer process from the dpm ligand to the Sm^{3+} ion, which has been experimentally identified for the

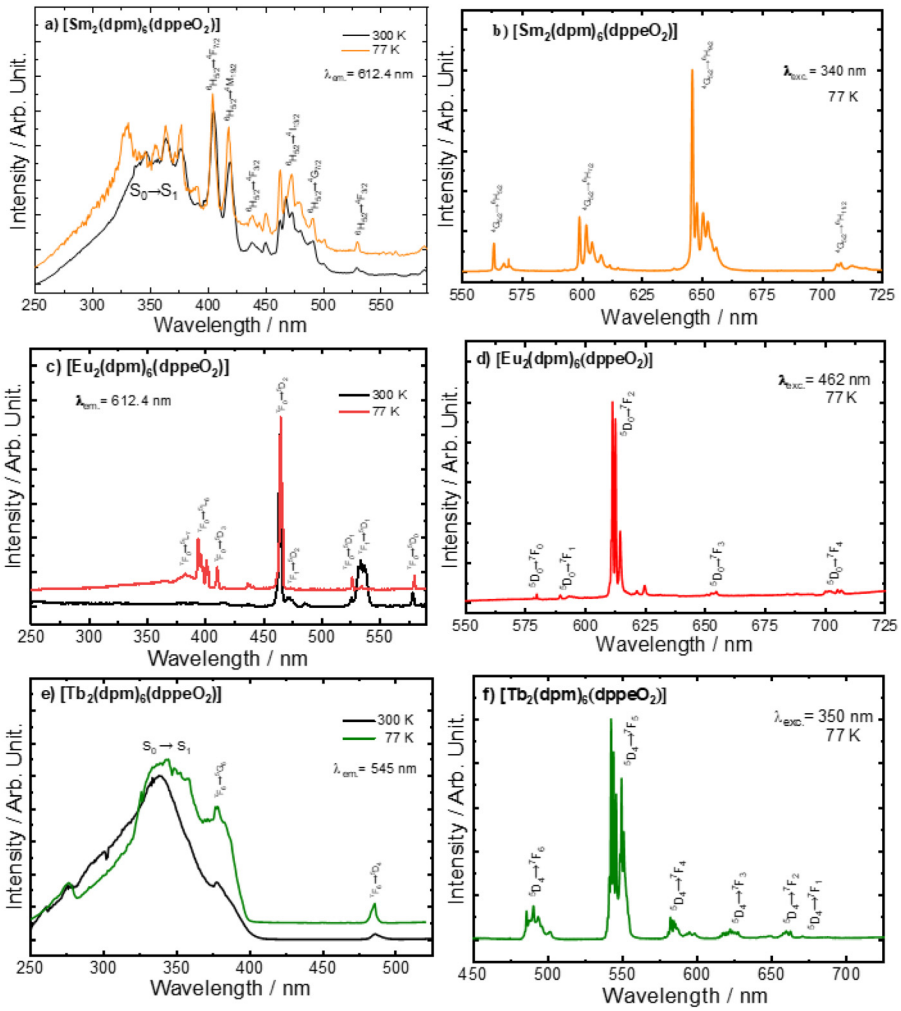

Fig. 3 (a) Excitation and (b) emission spectra of the $[Sm_2(dpm)_6(dppeO_2)]$ complex, (c) excitation spectra and (d) emission spectra of the $[Eu_2(dpm)_6(dppeO_2)]$ complex and (e) excitation spectra and (f) emission spectra of the $[Tb_2(dpm)_6(dppeO_2)]$ complex in the solid state.

$[Sm_2(dpm)_6(dppeO_2)]$ compound due to the efficient energy back-transfer processes.

The emission spectrum of the Sm^{3+} compound was recorded in the range from 420 to 720 nm (Fig. 3b and Fig. S7a†) at 298 K with excitation at 340 nm. The emission spectrum of this compound is characterized by narrow bands assigned to the $^4G_{5/2} \rightarrow {}^6H_J$ (J: 5/2, 7/2, 9/2, and 11/2) transition of the Sm^{3+} ion. It is important to highlight that the spectrum presents no broad phosphorescence ligand band. However, this behavior is not necessarily assigned to an efficient antenna effect in this compound. As mentioned above, energy back-transfer processes may also be quite efficient in this compound. The absolute quantum yield data corroborate this observation (Q^L_{Sm} = 0.5%) determined at room temperature. An analysis of the theoretical results presented below provides a better understanding of these results.

Fig. 3c shows the excitation spectra of the Eu^{3+} compound recorded at 300 and 77 K and monitored at the $^5D_0 \rightarrow {}^7F_2$ transition (611.4 nm), which indicate the absence of broad excitation bands of the dpm ligand compared to those of the Sm^{3+} (Fig. 3a) and Tb^{3+} (Fig. 3e) ions in high energy regions. Besides, the absence of narrow excitation peaks recorded at room temperature (Fig. 3e, black line) is noted, attributed to the intraconfigurational 4f transitions of the Eu^{3+} ion. On the other hand, the excitation spectra recorded at lower temperature (77 K, Fig. 3c, red line) exhibit narrow peaks at around 382, 394, and 415 nm assigned to the intraconfigurational $4f^6$ $^7F_0 \rightarrow {}^5L_7$, $^7F_0 \rightarrow {}^5L_6$ and $^7F_0 \rightarrow {}^5D_3$ transitions of the Eu^{3+} ion, respectively. Besides, the other $4f^6$–$4f^6$ transitions at $^7F_0 \rightarrow {}^5D_0$ (578 nm), $^7F_1 \rightarrow {}^5D_1$ (533 nm), $^7F_0 \rightarrow {}^5D_1$ (524 nm), $^7F_1 \rightarrow {}^5D_2$ (485 nm), and $^7F_0 \rightarrow {}^5D_2$ (463 nm), in which the highest intense band at 463 nm is attributed to the $^7F_0 \rightarrow {}^5D_2$ transition, in both excitation spectra are observed at 300 and 77 K. The excitation spectrum recorded at a lower temperature reveals some significant changes compared with the spectral data obtained at 300 K. Firstly, the intensities of the transitions arising from the $^7F_1$ level were significantly decreased due to the decrease in the thermal population at this level. Also, a slight baseline increase is observed in the highest energy region due to the broadband $S_0 \rightarrow S_n$ absorption transition. These optical changes occur in the same spectral region where the LMCT has been observed in the diffuse reflectance spectra (Fig. 2). Consequently, these findings suggest that the dpm charge transfer state acts as an efficient luminescence quencher, decreasing the population of organic ligands and Eu^{3+} excited states of higher energies.

The emission spectra of the Eu^{3+} compound, as shown in Fig. 3d, were recorded under direct excitation at 464 nm attributed to the $^7F_2 \rightarrow {}^5D_2$ transition centered on the Eu^{3+} ion regarding the very low excitation intensity of the ligand $S_0 \rightarrow S_1$ transition due to the excitation band suppression by the LMCT state. The emission measurements were carried out at 300 and 77 K (Fig. 3d and Fig. S7b†). It is worth noting that the emission spectra exhibit similar profiles, except for the higher spectral resolution for the one recorded at a lower temperature, suggesting that there are no significant structural changes when the temperature decreases. In addition, emission spectra display narrow bands assigned to the typical $^5D_0 \rightarrow {}^7F_J$ transitions (J = 0, 1, 2, 3, and 4), in which the band due to the $^5D_0 \rightarrow {}^7F_2$ transition (~611 nm) is the most prominent one. Moreover, these emission bands are split into approximately $2J + 1$ components, suggesting that the Eu^{3+} ion occupies a single chemical environment with symmetry belonging to the C_{2v} point group, corroborating the SHAPE analysis performed based on the crystallographic data.[30]

Luminescence decay curves of the $[Eu_2(dpm)_6(dppeO_2)]$ compound were also recorded at 300 and 77 K under excitation, and emission was monitored at 464 and 611.4 nm (Fig. S8a and b†), respectively. These curves were fitted with the monoexponential equation $I(t) = I_0 \exp(-t/\tau)$. Interestingly, the lifetime values of the compound at room temperature (τ = 0.387 ms) and liquid nitrogen temperature (τ = 0.424 ms) are similar. The lifetime values agree with the emission spectral data, indicating only one site symmetry in the chemical environment of the Ln^{3+} ion. This result indicates no significant temperature dependence of τ values, corroborating the diffuse reflectance and phosphorescence data showing the low-lying LMCT state between the ligand S_1 and T_1 excited states. Therefore, the LMCT state does not act as an efficient luminescence quencher in depopulating the emitting $^5D_0$ level of the Eu^{3+} ion, that is corroborated by the photoluminescence data observed for other Eu^{3+} complexes previously investigated by our group.[8] It is worth noting that the LMCT state can usually act as a more efficient quenching pathway when it is closer to the $^5D_0$ emission level, where the lifetime observed for the emitting $^5D_0$ level recorded at room temperature is about ten times smaller than that measured at liquid nitrogen temperature.[13,15]

Due to the uniqueness of the electronic transitions centered on the Eu^{3+} ion, experimental quantitative analyses are generally performed based on spectral data. In this case, the spontaneous Einstein emission coefficients ($A_0 \rightarrow J$) for the $^5D_0 \rightarrow {}^7F_J$ transitions and experimental Judd–Ofelt intensities (Ω_2 and Ω_4) may be directly obtained from the emission data. This issue has been extensively reported in ref. 33 and 34. Furthermore, the total decay rate (A_{total}) may be determined using the relationship $1/\tau = A_{total} = A_{rad} + A_{nrad}$. The intrinsic emission quantum yield can be estimated from these values using the following equation.[35]

$$Q^{Eu}_{Eu} = \frac{A_{rad}}{A_{tot}} = A_{rad}\tau \quad (1)$$

The following values were obtained for the $[Eu_2(dpm)_6(dppeO_2)]$ compound: the total radiative (A_{rad} = 1064 s^{-1}) and nonradiative (A_{nrad} = 1513 s^{-1}) rates, the Judd–Ofelt intensity parameters (Ω_2 = 26.8 × 10^{-20} cm^2; Ω_4 = 7.3 × 10^{-20} cm^2), the intrinsic emission quantum yield (Q^{Eu}_{Eu} = 41.2%) and the value for the absolute quantum yield (Q^L_{Eu} = 7%) determined at room temperature.

For the experimental data of the $[Eu_2(dpm)_6(dppeO_2)]$ compound, both absolute (Q^L_{Eu}) and intrinsic (Q^{Eu}_{Eu}) quantum yields were determined. In this case, the luminescence sensitization efficiency may be obtained as follows: $Q^L_{Eu} = \eta_{sens} \times Q^{Eu}_{Eu}$ = ; $\eta_{sens} = Q^L_{Eu}/Q^{Eu}_{Eu}$. The low value of $\eta_{sens} \approx 7\%$ is reflected by high

luminescence quenching due to the operative energy transfer process involving centered S_1 and T_1 ligand excited states and the LMCT state of low energy. These results are quite in agreement with theoretical data. It is worth mentioning that η_{sens} values were not determined for the other complexes since their intrinsic quantum yields may not be obtained directly from emission data.

The high value of the Ω_2 parameter reflects the strong emission intensity of the $^5D_0 \rightarrow {}^7F_2$ transition, which may be mainly correlated to higher angular distortions in the chemical environment of the Eu^{3+} ion. On the other hand, the low value of the Ω_4 parameter gives evidence that agrees with the slight covalency of Eu^{3+}–ligating atom interactions.[8,35] In this work, the LMCT state plays a minor role in the depopulation of the emitting $^5D_0$ level because the luminescence decay data at different temperatures are similar. The high A_{nrad} value suggests that multiphonon nonradiative contributions from the highly flexible dinuclear compounds with a bridging $dppeO_2$ ligand are likely the most operative deactivation channels. However, the radiative rate (A_{rad}) is also relatively high for this complex, leading to a high value of the intrinsic emission quantum yield (Q^{Eu}_{Eu}). On the other hand, the absolute quantum yield (Q^{L}_{Eu} = 7%) is very low compared to those of other Eu^{3+}–diketonate complexes, indicating that only a slight percentage of absorbed energy by the complex leads to radiation emission by the metallic center. This result suggests efficient luminescence quenching through the LMCT state, which efficiently depopulates the singlet and triplet states of the dpm ligand. To further investigate the energy transfer mechanisms for this complex, theoretical calculations were performed based on recently developed models for lanthanide ion compounds.

For the Tb^{3+} compound, narrow excitation bands characteristic of the Tb^{3+} ion assigned to the $^7F_6 \rightarrow {}^5D_4$ (485 nm) and $^7F_6 \rightarrow {}^5G_6$ (377 nm) transitions are observed when the excitation spectra are recorded at 300 and 77 K, monitoring the emission in the $^5D_4 \rightarrow {}^7F_5$ transition at 549 nm (Fig. 3e). The $[Tb_2(dpm)_6(dppeO_2)]$ compound exhibits a higher relative intensity of the dpm ligand band than those narrow bands centered on the metal ion, suggesting a more efficient luminescence sensitization process *via* intramolecular energy dpm ligand → Tb^{3+} ion transfer.

Emission spectra (Fig. 3f and Fig. S7c†) of the Tb^{3+} compound exhibit only characteristic narrow bands assigned to the $^5D_4 \rightarrow {}^7F_J$ transitions (J = 6, 5, 4, 3, and 2), with the $^5D_4 \rightarrow {}^7F_5$ transition (~545 nm) being the most intense one responsible for their green emission color. Moreover, no broad emission bands from the intraligand transitions were observed, indicating that the intramolecular energy transfer from the dpm ligand to the Tb^{3+} ion is very efficient. This evidence corroborates the high absolute quantum yield value (Q^{L}_{Tb} = 52%) determined at room temperature.

3.4 Intramolecular energy transfer processes: theoretical approach

In this work, theoretical studies of the $[Eu_2(dpm)_6(dppeO_2)]$ dimeric compound in four stages were also discussed. First, its geometry was optimized by taking as the starting geometry that obtained from X-ray diffraction experimental data. In this case, density functional theory (DFT) calculations were performed at the B3LYP/def2-SVP level for all H, C, N, O, and P atoms. For the Eu^{3+} ion, the effective core potential (ECP) was used with the remaining electrons as the valence basis set [7s 6p 5d]/[5s 4p 3d]-GTO.[36] A comparison between the initial and optimized geometries showed a root mean square deviation (RMSD) adjustment of approximately 1.009 Å, indicating similar structural features (Fig. 4). Furthermore, no imaginary vibrational frequencies were also found, suggesting that the obtained theoretical structure corresponds to a global energy minimum. Notably, the most significant deviations are observed in the *tert*-butyl groups of the dpm ligand. This finding can be attributed to the higher degrees of freedom inherent in these ligands, leading to more pronounced distortions in the overall geometry. By taking into account solely the coordination polyhedron, as shown in Fig. 4b, the RMSD value decreases to 0.440 Å, reinforcing theoretical calculations that describe the symmetry around the Eu^{3+} ion quite well.

In the second stage, the spectroscopic properties of the $[Eu_2(dpm)_6(dppeO_2)]$ compound were theoretically investigated based on the optimized geometry using time-dependent (TD-DFT) calculations. The calculations were carried out with the CAM-B3LYP functional, in which the Eu^{3+} ion was described by the Stuttgart–Dresden "large core" MWB52 and its remaining electrons as the valence basis set [7s 6p 5d]/[5s 4p 3d]-GTO. All H, C, N, O and P atoms were described at the B3LYP/def2-SVP[37] level. All DFT/TD-DFT calculations were performed using Orca 5.0.4 software.[38,39] As can be observed in Fig. S9,† the transitions in the 175–275 nm range with oscillator strengths of $f_{osc.}$ = 0.0074 and 0.0037, may be attributed to the $S_0 \rightarrow S_2$ (47 854 cm^{-1}) and $S_0 \rightarrow S_1$ (39 874 cm^{-1}) transitions of the dpm ligand. Compared with the experimental spectrum (Fig. 2, red line), the observed blue shifting is probably due to the intermolecular interactions not being considered in the theoretical approaches. Additionally, the energy of the low-lying excited triplet state (~24 961 cm^{-1}) was deter-

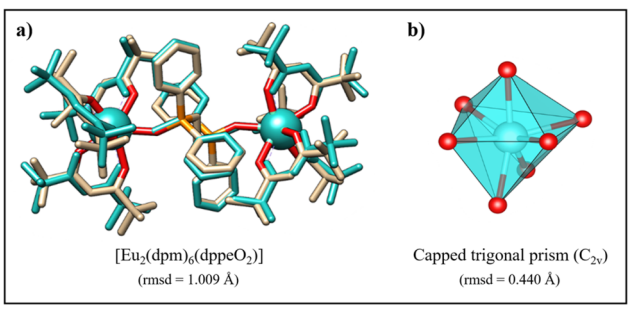

Fig. 4 (a) An overlay of the theoretical and experimental structures for the $[Eu_2(dpm)_6(dppeO_2)]$ compound. The carbon atoms in the theoretical structure are shown in cyan, while those in the experimental structure are shown in gray (hydrogen positions are excluded from the RMSD calculations). (b) Coordination polyhedron of the $[Eu_2(dpm)_6(dppeO_2)]$ compound optimized by DFT calculations.

mined assuming vertical transitions. The higher contributions for these transitions came from monoelectronic molecular orbitals located at a complex unit as a starting level to the molecular orbitals delocalized on the dimeric compound, as depicted in Fig. S14.†

Based on the compositions of the molecular orbitals (Fig. S14†), the distance (R_L) between the energy donor excited S_1 and T_1 states centered on the ligands and the Eu^{3+} acceptor ion was also theoretically determined for the $[Eu_2(dpm)_6(dppeO_2)]$ compound, following the procedure described by Moura Jr. *et al.*[40] The R_L values for this compound are ~3.55 Å for both the singlet and triplet states. It is worth mentioning that this value was also taken into account to calculate the energy transfer rates for the Sm^{3+} and Tb^{3+} compounds since the ligand–metal interactions in the $[Ln_2(dpm)_6(dppeO_2)]$ dimeric compounds are very similar, concerning that the ligand electronic structures are almost insensitive to the change in the Ln^{3+} ion.

In addition to the excited singlet and triplet states of the dpm ligand, it was possible to determine the contributions of ligand–metal (LMCT) and metal–ligand (MLCT) charge transfer states. The calculations were performed in the TD-DFT state using the CAM-B3LYP functional and the relativistic Hamiltonian DKH2. In this case, a more complete energy level structure for studying the dynamics of the intramolecular ligand-to-metal energy transfer process may be obtained.[41] Fig. 5a shows the main contributions of a series of excited states of the Eu complex. As can be seen, the lowest energy states have almost pure contributions from Eu^{3+} ion levels. The states located at around 20 000 cm^{-1} assume the ligand-centered state (LC) character.[42] The transition positions and the oscillator strengths involving these excited states are similar to those performed in non-relativistic calculations (Fig. 5a). In addition, many states with high ligand–metal charge transfer contributions are found at different energy values (Table S11†). Among the LMCT states, the lowest energy state is ~22 000 cm^{-1}, which can significantly influence the ligand-to-metal intramolecular energy transfer processes. Surprisingly, the lowest energy transition in the theoretical absorption spectra (Fig. S10†) is located in the same spectral region of the shoulder presented in the experimental diffuse reflectance spectrum of the $[Eu_2(dpm)_6(dppeO_2)]$ compound (Fig. 2, red line).

Fig. 5c displays the rendered orbitals for the $[Eu_2(dpm)_6(dppeO_2)]$ compound referring to the contributions to the transitions calculated at 22 264 and 25 928 cm^{-1}. Interestingly, the departure molecular orbitals are centered on the dpm ligand, while the arrival ones are centered on the Eu^{3+} ion. This result aligns well with experimental diffuse

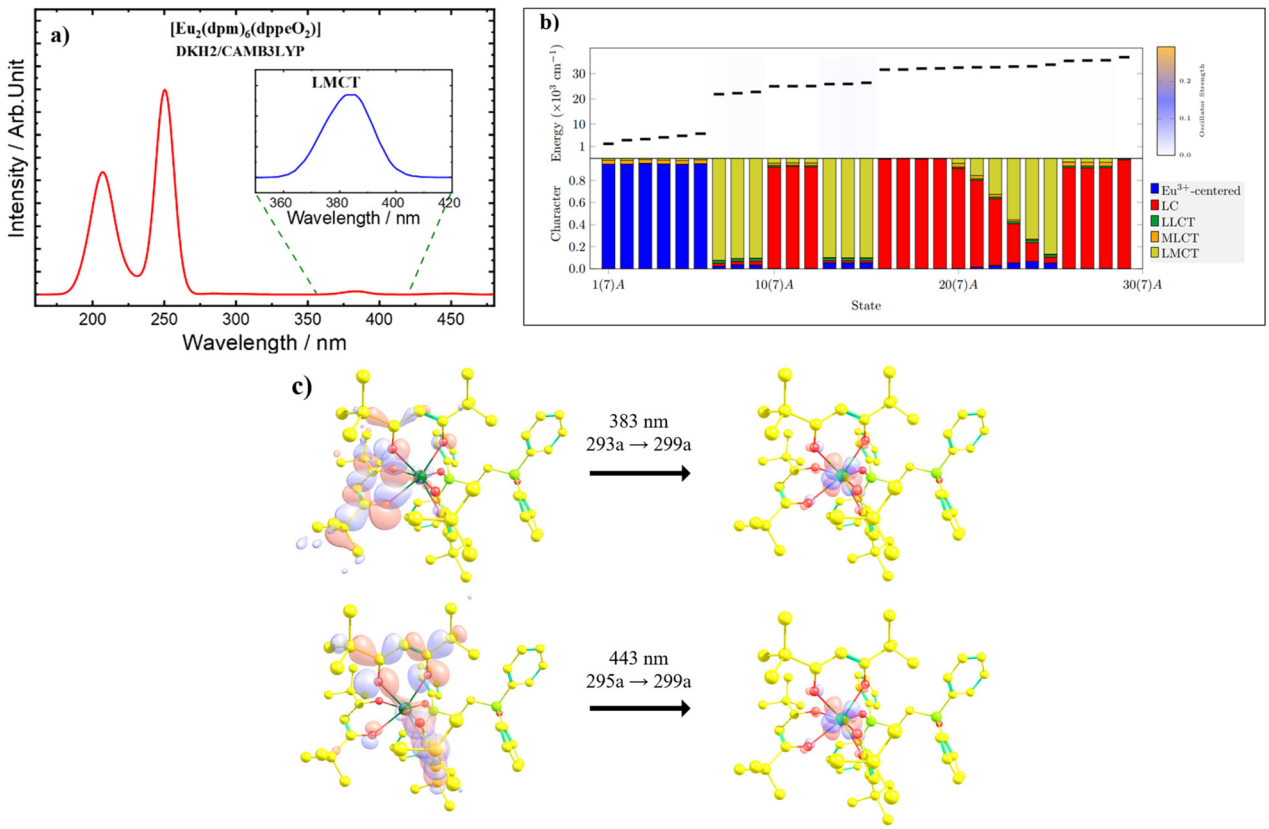

Fig. 5 (a) Absorption spectrum in the ultraviolet region obtained *via* TD-DFT calculations for the $[Eu_2(dpm)_6(dppeO_2)]$ coordination compound and (b) analysis of excited states using TheoDORE. (c) Compositions of the departure and arrival orbitals referring to the LMCT state of the $[Eu_2(dpm)_6(dppeO_2)]$ compound calculated at the TD-DFT/B3LYP/def2-SVP level, using the relativistic Hamiltonian DKH2.

reflectance data, supporting that the used theoretical approach is applicable for predicting the properties of the Eu^{3+} compound with ligand–metal charge transfer states localized at low energy positions. The rendered orbitals for the complexes containing Sm^{3+}, Gd^{3+} and Tb^{3+} that were used in the work are shown in Fig. S13–S16.†

Theoretical absorption data for the Sm^{3+}, Gd^{3+}, and Tb^{3+} compounds reveal similar spectral profiles to those for the analogous Eu^{3+} complex (Fig. S9, S11 and S12†) in the 150–340 nm range. Furthermore, these compounds present lower densities of charge transfer states in the low-energy spectral regions (Fig. S13–S16†). The theoretical spectra of the Sm^{3+} and Tb^{3+} complexes show the low-intensity bands from 340 to 500 nm, which exhibit higher contributions from LC or LLCT transitions, as can be observed from the data in Tables S10 and S13, and Fig. S13 and S16.† In this context, the LMCT and MLCT states play a minor role in the intramolecular ligand of the metal energy transfer processes in the $[Sm_2(dpm)_6(dppeO_2)]$ and $[Tb_2(dpm)_6(dppeO_2)]$ complexes. Interestingly, the Gd^{3+} complex shows only centered ligand transitions in all spectral regions, consistent with the experimental data (Fig. S15 and Table S12†).

Based on the structural data, the intensity parameters (Ω_λ), and the experimental energies of the ligand excited states, theoretical calculations were performed using the JoySpectra program[43] to determine the charge factors (g) and polarizabilities (α) of the ligating oxygen atoms coordinated to the Eu^{3+} ion (Table 2). Furthermore, the nonradiative intramolecular energy transfer (IET) rates among the ligand and lanthanide ion excited states were also determined. In these calculations, not only the excited ligand states were taken into account, but also the lowest energy LMCT state. The theoretical approaches are reported in ref. 10, 44 and 45. It is worth noting that the ligating atom polarizabilities (α) have the contributions of effective (α') and overlap (α_{OP}) polarizabilities, such that $\alpha = \alpha' + \alpha_{OP}$. Calculating the g and α' quantities considered the ligating oxygen atoms belonging to each dpm ligand classified into two groups, depending on the Eu–O bond lengths. Due to the difference in the P═O bonds compared to those in the dpm ligand, the oxygen atoms of the $dppeO_2$ ligand were considered a separate group. The g and α' values were adjusted to minimize the difference between the theoretical and experimental parameter values $\Omega_\lambda^{Theor.}$ and $\Omega_\lambda^{Exp.}$, where λ = 2, 4 and 6. The small difference between the values of these parameters (Table S7†) indicates a suitable parameter adjustment. Interestingly, the calculated values of g and α', as well as α_{OP} for the oxygen atoms belonging to the $dppeO_2$ ligand, are consistent with the highly polarized π-bond of the P═O moiety in the diphosphine oxide ligand to the oxygen atoms. Besides, the g and α' values for the oxygen atoms of the dpm ligand reveal that the shorter distance between Eu and O bonds (Table S4†) has higher values of these parameters than those in which the metal–donor atom bonds are longer. This finding suggests that the chemical environments around the Eu^{3+} ions in the dimeric Eu^{3+} compounds are highly polarizable, mainly provided by the oxygen atoms from $dppeO_2$ and those from the shorter Eu–O bonds due to the asymmetric coordination of the dpm ligand.

The forced electric-dipole contributions for Ω_λ parameters λ = 2, 4, and 6, determined from the JoySpectra equal to 0.133780, 0.249331, and 0.406451 × 10^{-20} cm^2, respectively, were used to calculate the rate equations associated with the ligand–metal intramolecular energy transfer mechanism of the Eu^{3+} compounds. The most significant values of IET rates for the electric dipole (W_{dd}), magnetic dipole (W_{md}), and exchange (W_{ex}) mechanisms are summarized in Table 2. As can be seen, the exchange mechanism dominates the energy transfer pathways from the singlet state, involving the $^7F_0 \rightarrow {}^5D_1$ and $^7F_0 \rightarrow {}^5G_2$ transitions of the Eu^{3+} ion. Notably, energy backward (W_B^S) processes involving the S_1 ligand state are inoperative. On the other hand, the $^7F_0 \rightarrow {}^5D_1$ and $^7F_1 \rightarrow {}^5G_2$ transitions also exhibit significant contributions in the energy backward processes to T_1 state of the ligand, presenting rate values of around 107 and 108 s^{-1}. Interestingly, a high backward energy (W_B^T) transfer rate value involving the $^7F_0 \rightarrow {}^5D_1$ transition for the Eu^{3+} complexes and dpm triplet state is an unexpected result. However, the energy of the low-lying T_1 of the dpm ligand in the Ln^{3+}-complexes is unusually low compared to other complexes with the same sensitizing ligand. A similar result has been reported by Pedro-Hasegawa *et al.*[17] for dimeric compounds with dppep2 ligand, in which the triplet state was located at ~20 000 cm^{-1}.

In this case, the data in Table 2 indicate that the main net pathway of luminescence sensitization involves the low-lying T_1 ligand state and $^7F_1 \rightarrow {}^5D_0$ transition of the Eu^{3+} ion. This optical behavior occurs even when the lowest energy LMCT state has been considered in the IET process. For the $[Eu_2(dpm)_6(dppeO_2)]$ compound, the LMCT state located at high energy (29 154 cm^{-1}) plays only a minor role in depopulating the excited T_1 ligand state and excited $^5D_0$ and $^5D_1$ levels

Table 2 Forward (W^S, W^T and W^{LMCT}) and backward (W_B^S, W_B^T and W_B^{LMCT}) intramolecular energy transfer (IET) rates (in s^{-1}) of the $[Eu_2(dpm)_6(dppeO_2)]$ complex

Intramolecular energy transfer	Rate, W (s^{-1})
Energy transfer from the S_1 state	
$S_1 \rightarrow (^7F_1 \rightarrow {}^5D_1)$	1.59×10^6
$S_1 \rightarrow (^7F_1 \rightarrow {}^5G_2)$	3.91×10^7
Back energy transfer from the S_1 state	
$S_1 \leftarrow (^7F_1 \rightarrow {}^5D_4)$	3.66×10^{-8}
$S_1 \leftarrow (^7F_1 \rightarrow {}^5G_4)$	2.59×10^{-8}
Energy transfer from the T_1 state	
$T_1 \rightarrow (^7F_0 \rightarrow {}^5D_1)$	4.74×10^9
$T_1 \rightarrow (^7F_0 \rightarrow {}^5D_0)$	9.96×10^8
Back energy transfer from the T_1 state	
$T_1 \leftarrow (^7F_0 \rightarrow {}^5D_1)$	9.84×10^7
$T_1 \leftarrow (^7F_0 \rightarrow {}^5D_2)$	1.76×10^8
Energy transfer from the LMCT state	
LMCT $\rightarrow S_1$	3.83×10^1
LMCT $\rightarrow T_1$	6.86×10^9
Back energy transfer from the LMCT state	
LMCT $\leftarrow S_1$	3.83×10^1
LMCT $\leftarrow T_1$	6.86×10^9
LMCT $\leftarrow (^7F_0 \rightarrow {}^5D_4)$	1.84×10^7

of the Eu^{3+} ion. The lower values for energy transfer rates $W(T_1 \rightarrow {}^5D_1) = 4.74 \times 109\ s^{-1}$ from these states agree with this hypothesis. Conversely, the energy transfer rate from the excited singlet (S_1) to the LMCT state is significantly high $W(S_1 \rightarrow \text{LMCT}) = 4.96 \times 1010\ s^{-1}$, indicating an efficient depopulation of this excited ligand state by the LMCT state, corroborating the absence of the broad bands of the excitation spectra in Fig. 3c. These data also agree with the theoretical predictions described in the work of Faustino *et al.*,[11] since the LMCT state has lower energy than the S_1 state, confirming the efficient luminescence quenching of Eu^{3+} compounds.[44] A simplified Jablonski diagram illustrating the intramolecular energy transfer in the $[Eu_2(dpm)_6(dppeO_2)]$ compound is illustrated in Fig. 6.

Considering the similar characteristics of the compounds investigated in this work, the *g* and α quantities for the oxygen atoms in the first coordination sphere for the Sm^{3+} and Tb^{3+} compounds were taken as those obtained for the analogous Eu^{3+} compound presented in Table S4.† From these data, the intensity parameters and energy transfer rates assigned to the intramolecular energy transfer processes were also calculated for the $[Sm_2(dpm)_6(dppeO_2)]$ and $[Tb_2(dpm)_6(dppeO_2)]$ compounds using the JoySpectra platform (Tables S5 and S6†).

Concerning all the luminescence sensitization processes, the calculated values of the energy transfer rates involving the excited S_1 state are significantly high for both the Sm^{3+} and Tb^{3+} dimeric compounds. However, in the case of the Tb complex, the backward rates involving these states are of the same order of magnitude (Tables S8 and S9†). This finding indicates that luminescence sensitization *via* the S_1 state is ineffective for Sm^{3+} and Tb^{3+} ions. Furthermore, there are efficient back energy transfers from the excited levels of both the Sm and Tb compounds to the low-lying triplet state. On the other hand, the high values of energy transfer rates $W(T_1 \rightarrow {}^5G_{5/2}\text{:Sm}) = 1.51 \times 10^9\ s^{-1}$ and $W(T_1 \rightarrow {}^5D_4\text{:Tb})\ 1.08 \times 10^9\ s^{-1}$ involving the low-lying T_1 state and the principal emitting

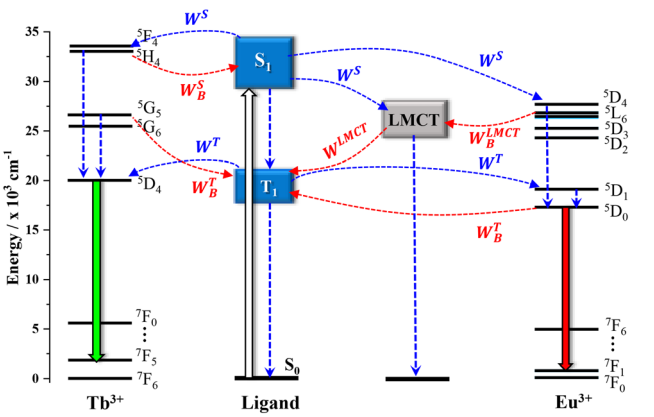

Fig. 6 Partial energy level diagram showing the primary energy transfer pathways for the $[Tb_2(dpm)_6(dppeO_2)]$ and $[Eu_2(dpm)_6(dppeO_2)]$ complexes. S_0, S_1 and T_1 are the ground, singlet and triplet excited states of the ligand, respectively.

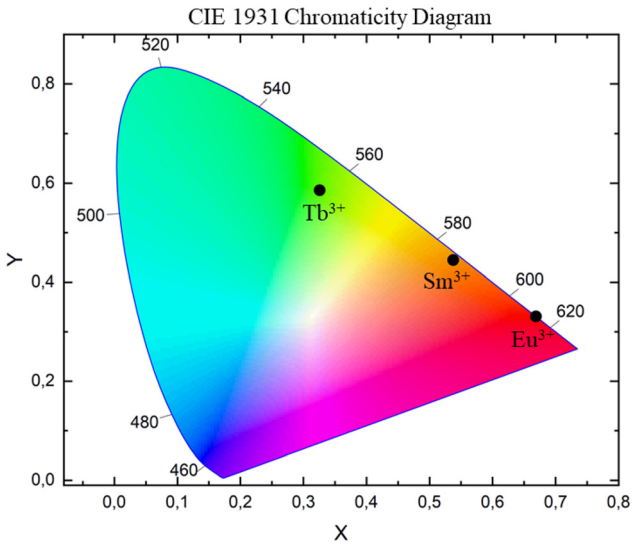

Fig. 7 CIE diagram of the $[Ln_2(dpm)_6(dppeO_2)]$ complexes (Ln^{3+}: Sm^{3+}, Eu^{3+}, and Tb^{3+}) in the solid state.

levels are consistent with most operative energy transfer pathways for the Sm^{3+} and Tb^{3+} compounds (Tables S8 and S9†). In addition, the Sm^{3+} compound has an efficient energy back-transfer process from the excited ${}^5G_{7/2}$ level to the T_1 state, which is found only slightly above the emitting ${}^5G_{5/2}$ level. This effect may contribute to the depopulation of the ${}^5G_{5/2}$ level, reducing the luminescence sensitization. As mentioned above, the energies of the first T_1 excited states of the dpm ligands are ~1760 cm^{-1} above the emitting ${}^4G_{5/2}$ state of the Sm^{3+} ion (Fig. S9†).

The CIE coordinate values (*x* and *y*) of the $[Sm_2(dpm)_6(dppeO_2)]$, $[Eu_2(dpm)_6(dppeO_2)]$ and $[Tb_2(dpm)_6(dppeO_2)]$ complexes were calculated from their emission spectra by using the CIE chromaticity coordinate diagram (Fig. 7).

4. Conclusions

In this work, four new luminescent lanthanide complexes $[Ln_2(dpm)_6(dppeO_2)]$ (Ln: Sm^{3+}, Eu^{3+}, Gd^{3+}, and Tb^{3+}) were successfully obtained. Excitation spectral data reveal a more efficient luminescence sensitization process for the Tb^{3+} system, whereas less operative sensitization processes for the analogous Sm^{3+} and Eu^{3+} compounds have been observed. The emission spectra of the $[Ln_2(dpm)_6(dppeO_2)]$ complexes exhibit only characteristic narrow bands arising from intraconfigurational $4f^N$ transitions, with ${}^4G_{5/2} \rightarrow {}^6H_{13/2}$ (Sm^{3+}), ${}^5D_0 \rightarrow {}^7F_2$ (Eu^{3+}) and ${}^5D_4 \rightarrow {}^7F_5$ (Tb^{3+}) being the dominant transitions. Theoretical calculations using the JoySpectra platform for the Tb^{3+} compound showed that the excited singlet S_1 state plays the most important role in sensitization. However, for the calculation of the Sm^{3+}compound, the IET processes involving the low-lying triplet T_1 state of the dpm ligand and the excited levels of the Sm^{3+} ion are the most operative pathways.

Furthermore, the energy back-transfer processes, including the same pathways, are also efficient, yielding a low net transfer process. The experimental values of intrinsic and absolute quantum yields for the Eu^{3+} compound reflect the presence of an operating luminescence quenching channel *via* the LMCT state. These optical results of the $[Eu_2(dpm)_6(dppeO_2)]$ complex are in agreement with the theoretical calculations, showing a high contribution of the luminescence quenching *via* intramolecular energy transfer rates from the S_1 to LMCT states.

Author contributions

The manuscript was written with the contributions of all authors. All authors have approved the final version of the manuscript. P. R. S. Santos: conceptualization, methodology, investigation, formal analysis, data curation, validation, visualization, writing – original draft, and writing – review & editing. A. A. S. S. Jesus: conceptualization, methodology, investigation, formal analysis, and data curation. W. B. Lima: conceptualization, methodology, investigation, formal analysis, and data curation. I. F. Silva: theoretical methodology, investigation, formal analysis, data curation, validation, visualization, and writing – review & editing. J. G. Arruda: methodology, investigation, formal analysis, and data curation. I. F. Costa: formal analysis, data curation, validation, visualization, and writing – review & editing. W. M. Faustino: resources, supervision, and writing – review & editing. M. C. F. C. Felinto: data curation, investigation, and writing – original draft. R. Diniz: data curation, investigation, and writing – original draft. H. F. Brito: data curation, investigation, and writing – original draft. E. E. S. Teotonio: conceptualization, funding acquisition, investigation, methodology, project administration, resources, supervision, writing – original draft, and writing – review & editing.

Data availability

The data supporting this article have been included as part of the ESI.†

Conflicts of interest

There are no conflicts to declare.

Acknowledgements

This work was funded by the Universidade Federal da Paraíba (PRODUTIVIDADE UFPB 03/2020, PVA13345-2020). The authors also thank Conselho Nacional de Desenvolvimento Científico e Tecnológico (CNPQ: 317047/2021-3) and Coordenação de Aperfeiçoamento de Pessoal de Nível Superior (CAPES) and Fundação de Amparo à Pesquisa do Estado de São Paulo (FAPESP: 2021/08111-2). The authors also acknowledge the computer resources provided by Centro Nacional de Processamento de Alto Desempenho em São Paulo (CENAPAD-SP). Proc n 2022/12709-3.

References

1 G. Figueiredo, S. F. H. Correia, L. Fu, V. Z. Bermudez, A. N. Carneiro Neto, P. S. André and R. A. S. Ferreira, in *Handbook on the Physics and Chemistry of Rare Earths*, Elsevier B.V., 2024, vol. 60, pp. 55–162.
2 S. Bhuckory, S. Lahtinen, N. Höysniemi, J. Guo, X. Qiu, T. Soukka and N. Hildebrandt, *Nano Lett.*, 2023, **23**, 2253–2261.
3 Y. Song, M. Lu, G. A. Mandl, Y. Xie, G. Sun, J. Chen, X. Liu, J. A. Capobianco and L. Sun, *Angew. Chem., Int. Ed.*, 2021, **60**, 23790–23796.
4 I. F. Costa, L. Blois, T. B. Paolini, I. Assunção, E. E. S. Teotonio, M. C. F. C. Felinto, R. T. Moura Jr., R. L. Longo, W. M. Faustino, L. D. Carlos, O. L. Malta, A. N. C. Neto and H. F. Brito, *Coord. Chem. Rev.*, 2024, **502**, 215590.
5 A. N. Carneiro Neto, E. E. S. Teotonio, G. F. de Sá, H. F. Brito, J. Legendziewicz, L. D. Carlos, M. C. F. C. Felinto, P. Gawryszewska, R. T. Moura, R. L. Longo, W. M. Faustino and O. L. Malta, in *Handbook on the Physics and Chemistry of Rare Earths*, Elsevier B.V., 2019, pp. 55–162.
6 J. L. Moura, I. F. Costa, P. R. S. Santos, I. F. Silva, R. T. Moura, A. N. Carneiro Neto, W. M. Faustino, H. F. Brito, J. R. Sabino and E. E. S. Teotonio, *Inorg. Chem.*, 2022, **61**, 13510–13524.
7 P. R. S. Santos, A. A. S. S. Jesus, W. B. Lima, J. G. Arruda, W. M. Faustino, M. C. F. C. Felinto, J. R. Sabino, H. F. Brito, I. F. Costa, R. T. Moura, A. N. Carneiro Neto, O. L. Malta, H. Terraschke and E. E. S. Teotonio, *Eur. J. Inorg. Chem.*, 2024, **27**, e202300660.
8 D. Xia, J. Li, M. Gao, T. Zhou, S. Zhao, J. Zhang and G. Li, *Inorg. Chim. Acta*, 2023, **556**, 121633.
9 A. N. Carneiro Neto, R. T. Moura and O. L. Malta, *J. Lumin.*, 2019, **210**, 342–347.
10 G. B. Zhou and D. Yan, *Adv. Funct. Mater.*, 2023, **33**, 2300735.
11 C. Xing, Z. Qi, Y. J. Ma, D. Yan and W. Fang, *Angew. Chem., Int. Ed.*, 2025, e202502782.
12 W. M. Faustino, O. L. Malta and G. F. de Sá, *Chem. Phys. Lett.*, 2006, **429**, 595–599.
13 M. T. Berry, P. S. May, H. Xu and J. Phys, *Chem*, 1996, **100**, 9216–9222.
14 F. Fulgêncio, F. C. De Oliveira, F. F. Ivashita, A. Paesano, D. Windmöller, A. Marques-Netto, W. F. Magalhães and J. C. MacHado, *Spectrochim. Acta, Part A*, 2012, **92**, 415–418.
15 F. Fulgêncio, A. S. Borges, J. G. Da Silva, T. Ribeiro, R. Diniz, D. Windmöller, M. H. Araujo and W. F. Magalhães, *AIP Conf. Proc.*, 2019, **2182**, 050029.

16 Y. C. Miranda, L. L. A. S. Pereira, J. H. P. Barbosa, H. F. Brito, M. C. F. C. Felinto, O. L. Malta, W. M. Faustino and E. E. S. Teotonio, *Eur. J. Inorg. Chem.*, 2015, **2015**, 3019–3027.
17 K. Yanagisawa, Y. Kitagawa, T. Nakanishi, K. Seki, K. Fushimi, H. Ito and Y. Hasegawa, *Chem. - Eur. J.*, 2018, **24**, 1956–1961.
18 Y. Kitagawa, M. Kumagai, P. P. Ferreira da Rosa, K. Fushimi and Y. Hasegawa, *Chem. – Eur. J.*, 2021, **27**, 264–269.
19 T. Fujii, Y. Kitagawa, Y. Hasegawa, H. Imoto and K. Naka, *Inorg. Chem.*, 2022, **61**, 17662–17672.
20 Y. Kitagawa, M. Kumagai, K. Fushimi and Y. Hasegawa, *Chem. Phys. Lett.*, 2020, **749**, 749137437.
21 Y. Hirai, T. Nakanishi and Y. Hasegawa, *J. Lumin.*, 2016, **170**, 801–807.
22 E. E. S. Teotonio, H. F. Brito, M. Cremona, W. G. Quirino, C. Legnani and M. C. F. C. Felinto, *Opt. Mater.*, 2009, **32**, 345–349.
23 *Rigaku Oxford DiffractionAgilent Technologies -, CrysAlisPro Data Collection and Processing Software for Agilent X-Ray Diffractometers*, 2014.
24 O. V. Dolomanov, L. J. Bourhis, R. J. Gildea, J. A. K. Howard and H. Puschmann, *J. Appl. Crystallogr.*, 2009, **42**, 339–341.
25 L. J. Farrugia, An update, *J. Appl. Crystallogr.*, 2012, **45**, 849–854.
26 *POV-Ray. Persistence of Vision Raytracer, Version 3.6*, 2004.
27 K. Momma and F. Izumi, *J. Appl. Crystallogr.*, 2008, **41**, 653–658.
28 H. Yan, Z. W. Che and W. Bin Sun, *New J. Chem.*, 2002, **47**, 140–146.
29 M. Seitz, A. G. Oliver and K. N. Raymond, *J. Am. Chem. Soc.*, 2007, **129**, 11153–11160.
30 D. Casanova, M. Llunell, P. Alemany and S. Alvarez, *Chem. – Eur. J.*, 2005, **11**, 1479–1494.
31 S. Sankar and K. G. Warrier, *J. Solgel Sci. Technol.*, 2001, **58**, 195–200.
32 P. R. S. Santos, D. K. S. Pereira, I. F. Costa, I. F. Silva, H. F. Brito, W. M. Faustino, A. N. Carneiro Neto, R. T. Moura, M. H. Araujo, R. Diniz, O. L. Malta and E. E. S. Teotonio, *J. Lumin.*, 2020, **226**, 117455.
33 G. S. Ofelt, *J. Chem. Phys.*, 1963, **38**, 2171–2180.
34 B. R. Judd, *Phys. Rev.*, 1962, **127**, 750–761.
35 J.-C. G. Bünzli, *Coord. Chem. Rev.*, 2015, **293–294**, 19–47.
36 F. Weigend and R. Ahlrichs, *Phys. Chem. Chem. Phys.*, 2005, **7**, 3297–3305.
37 M. Dolg, H. Stoll and H. Preuss, *Theor. Chim. Acta*, 1993, **85**, 441–450.
38 F. Neese, The ORCA program system, *Wiley Interdiscip. Rev.: Comput. Mol. Sci.*, 2012, **2**, 73–78.
39 F. Neese, Software update: the ORCA program system, version 4.0, *Wiley Interdiscip. Rev. Comput. Mol. Sci.*, 2018, **8**, e1327.
40 R. T. Moura Jr, A. N. Carneiro Neto, R. L. Longo and O. L. Malta, *J. Lumin.*, 2016, **170**, 420–430.
41 J. G. Arruda, I. F. Silva, W. M. Faustino, I. F. Costa, H. F. Brito, A. N. Carneiro Neto, C. Nather, H. Terraschke, M. C. F. C. Felinto, V. M. Deflon and E. E. S. Teotonio, *Polyhedron*, 2025, **267**, 117313.
42 F. Plasser, TheoDORE: A toolbox for a detailed and automated analysis of electronic excited state computations, *J. Chem. Phys.*, 2020, **152**, 084108.
43 R. T. Moura, A. N. Carneiro Neto, E. C. Aguiar, C. V. Santos, E. M. de Lima, W. M. Faustino, E. E. S. Teotonio, H. F. Brito, M. C. F. C. Felinto, R. A. S. Ferreira, L. D. Carlos, R. L. Longo and O. L. Malta, *Opt. Mater.*, 2021, **11**, 100080.
44 W. M. Faustino, O. L. Malta and G. F. De Sá, *J. Chem. Phys.*, 2005, **122**, 054109.
45 W. M. Faustino, O. L. Malta, E. E. S. Teotonio, H. F. Brito, A. M. Simas and G. F. De Sa, *J. Phys. Chem. A*, 2006, **110**, 2510–2516.